Determination of effective stress intensity factors under mixed-mode from digital image correlation fields in presence of contact stresses and plasticity

Thomas Bonniot, Véronique Doquet, Si Hai Mai

Determination of effective Stress Intensity Factors under mixed-mode from DIC fields in presence of contact stresses and plasticity

Thomas Bonniot *[1,2], Véronique Doquet [1], Si Hai Mai [2]

[1]Laboratoire de Mécanique des Solides,
CNRS, UMR 7649, Ecole Polytechnique, 91120 Palaiseau, France
[2]SNCF Innovation and Research,
1-3 avenue François Mitterrand, 93210 Saint-Denis, France

* Corresponding author: *Email adress:* thomas.bonniot@polytechnique.edu

Abstract

Digital Image Correlation (DIC) is more and more popular to monitor fatigue crack growth and to determine the stress intensity factors. However, the post-treatment of the recorded displacement fields becomes tricky when the crack faces are not stress-free and when crack tip plasticity becomes significant. Several post-treatment methods to locate the crack tip and measure the effective SIFs in such cases are compared, using FEM-computed displacement fields, and then used on real DIC fields. An approach coupling DIC and FEM is proposed to estimate the contact stresses along the crack.

Keywords: *Fatigue crack, mode II, mode I+II, contact, friction, DIC, Crack-tip plasticity, non-proportional mixed mode*

1 Introduction

When investigating fatigue crack growth, several methods can be used to monitor crack growth and to measure the effective stress intensity factors (SIFs), allowance made for closure effects, in mode I, and friction effects, in mode II and III. The crack length can be measured using a compliance variation method, or the DC potential drop method, direct surface imaging with a camera, or indirect imaging on replicas, or crack propagation resistive gages. Some of those methods are time consuming or difficult to calibrate, especially in mixed-mode, or when bifurcation occurs. In order to evaluate the effective SIFs, one can for example detect a change in stiffness on the tensile force-opening displacement loop, in mode I, or on the shearing force-sliding displacement loop in mode II [1, 2].

Digital image correlation, which is fast (for the experimental part) and does not require sophisticated devices, has been used a lot recently to locate the crack tip and to evaluate the effective SIFs. Since the speckle pattern makes a direct measurement of the crack length difficult, the DIC displacement fields are generally used to evalute both the crack tip position and the effective SIFs, using methods often based on LEFM, which supposes no plasticity and no contact stresses between the crack faces. This article deals with the feasibility of such techniques in the presence of high contact stresses and high plasticity/loading ranges in mixed mode.

The principle of using an experimentally-determined displacement field to evaluate the SIFs was proposed by Barker et al. [3] in 1985, with a displacement field computed from the stress field obtained by photo-elasticity. The experimental displacement field was projected over a theoretical displacement field (obtained from Westergaard's equations), and the crack tip position was supposed to be known. The SIFs were computed from the resulting coefficients. A similar approach was then used by Abanto-Bueno

& Lambros [4] on a displacement field obtained by DIC, and has been used widely since then.

This approach based on a projection on William's expansion (or another analytical displacement field, such as Westergaard's solutions) was used in [3, 4, 5, 6] with a crack tip position supposed to be known.

Others used this method to evaluate both the crack tip position and the SIFs, by seeking the position of the crack tip which minimizes the error between the DIC field and its projection on the theoretical field. Roux & Hild [7] used this principle, without giving further details on the method. Yoneyama et al. [8] tried to optimize simultaneously the value of the SIFs and the crack tip position using a Newton-Raphson method, which as Zanganeh et al. [9] pointed out, is very sensitive to the initial guess of the crack tip position. Zanganeh et al. [9] used numerically generated or experimentally obtained displacement fields to perform a comparative study on various methods: two Newton-type methods, a simplex method, a genetic algorithm and a Pattern Search method. This last method was found to be satisfying, both in terms of accuracy and computational cost. Harilal et al. [10] tried every possible position of the crack tip on a square grid, which has the advantage of avoiding convergence towards a local minima, but is not very efficient in terms of computational cost, especially since the grid pitch has to be small to get a precise estimation. Vormwald et al. [11] tried a similar approach, but with grids of varying size: a first estimation of the crack tip position is found using a coarse grid, then the process is repeated on a refined grid around the previously estimated crack tip. This process can be repeated as many times as necessary to get an accurate estimate of the crack tip position.

Some authors used a projection on a theoretical field, but with a different way to locate the crack tip, such as Lopez-Crespo et al. [12, 13] who applied a Sobel line detection algorithm to the DIC displacement field to locate the crack tip. Hamam et al. [14] as well as Mathieu et al. [15] added supersingular terms (terms of negative order) to William's expansion. It was then possible to locate the crack tip by seeking the position where the -1 order term was equal to zero.

Other methods, not involving a projection over a theoretical field, were used by some authors. Réthoré et al. [16, 17] used an interaction integral to evaluate the SIFs, but such method supposes stress-free crack faces. Roux et al. [7, 14, 15] used an integrated approach, where shape functions corresponding to a theoretical displacement field for an elastic cracked body were used in the image correlation process.

In all the aforementioned methods, only the displacements measured outside the crack tip plastic zone and the plastic wake were taken into account in the analysis, but crack tip plasticity was not taken into account in the analytical displacement fields used to determine the SIFs, except in [14, 15] in a very simplified way.

Hos et al. [18] used the relative opening displacement measured between two points on each side of the crack (COD) and estimated crack closure using the stifness change method on the displacement jump - force loop. Vormwald et al. [11] used the same displacement jump measurements to get a direct estimate of the SIFs, knowing the analytical relationship between those two values. The same type of approach was used by Smith & Smith [1] using an extensometer to measure the crack sliding displacement, and by Wong et al. [19, 20] using surface replicas to measure the displacement jump. By contrast, Bertolino & Doquet [2] compared the measured sliding displacement profiles to those issued from elastic-plastic simulations, with or without a uniform friction stress along the crack face.

Decreuse et al. [21] proposed a different approach, where the plasticity-free mode I and mode II displacement fields are not analytical, but obtained from DIC by correlating an image taken at maximum load and an image taken after a small, fully elastic unloading. A second displacement field, containing the influence of crack tip plasticity, can also be built by correlating images obtained during a monotonic loading and subtracting the elastic part obtained previously. The four fields (two for each mode) are then used in the same way as the analytical displacement fields in the previous projective approaches.

Bertolino & Doquet [2], Doquet et al. [22] & Bonniot et al. [23] compared the measured in-plane or out-of-plane crack face relative sliding displacement profiles to those issued from elastic-plastic FEM computations run with various loading ranges, to find the loading range which gives the best fit of experimental data. The effective ΔK_{II} or ΔK_{III} were deduced from the corresponding loading range.

The experimental conditions of all those papers are summarized in table 1.

Table 1: Test conditions found in the literature. COD stands for the measurement of the displacement jump between two points. DJ stands for the measurement of the displacement jump between two lines. If the displacement field are not obtained from DIC, the method is given in parenthesis. I/II means proportional mixed mode and $I + II$ non-proportional mixed mode.

Authors	Material	Mode	R_I	Method for SIF measurement	Crack-tip plasticity modelling?
Abanto [4]	polyethylene	I	(0, not fatigue)	Analytical full field	no
Réthoré [16]	maraging steel	I/II	0	interaction integral	no
Réthoré [17]	SiC	I	(0, not fatigue)	interaction integral	no
Roux [7]	SiC	I	(0, not fatigue)	DIC integrated	no
Roux [7]	SiC	I	(0, not fatigue)	Analytical full field	no
Yoneyama [8]	PMMA	I/II	(0, not fatigue)	Analytical full field	no
Hamam [14]	Steel	I	0	Analytical full field	simplified
Hamam [14]	Steel	I	0	DIC integrated	no
Lopez Crespo [12, 13]	7010 Al	I/II	0	Analytical full field	no
Yates [5]	7010 Al	I	>0.15	Analytical full field	no
Mathieu [15]	Ti35	I	0.1	Analytical full field	simplified
Zanganeh [9]	Al (2 types)	I/II	0	Analytical full field	no
Harilal [10]	2014-T6 Al	I/II	≥ 0	Analytical full field	no
Lachambre [24]	Iron	I	0.14	Analytical full field	no
Hos [18]	S235	I+II	-1	COD	no
Vormwald [11]	S235	I+II	-1	COD	no
Vormwald [11]	S235	I+II	-1	Analytical full field	no
Tong [6]	316L	I	0.1	Analytical full field	no
Decreuse [21]	S355	I+II	>0	DIC basis	yes
Bertolino [2]	M250 & Ta6V	II	/	DJ (SEM insitu)	yes
Doquet [22]	M250 & Ta6V	II/III	/	DJ (replicas)	yes
Bonniot [23]	R260	II/III	/	DJ	yes
Wong [19, 20]	Rail steel	I+II	0	COD (replicas)	no

From this literature survey, it appears that except in [18, 11], DIC analysis of fatigue crack growth was always applied for zero or positive mode I R ratios. For negative R ratios, it would be tempting to correlate the images captured at peak load and zero load, ignoring the compressive part of the cycle. However, crack closure sometimes occurs in compression and part of the compressive stage of the cycle sometimes contributes to crack growth [25], so that a strategy for the post-treatment of DIC fields is needed in presence of a compressive stage. Furthermore, in mixed mode, normal compression enhances contact and friction stresses along the crack and no theoretical expression of the displacement field is available in that case.

Fatigue cracks in rails undergo non-proportional mixed-mode loading with compression phases [26, 27]. The loading paths are approximately sequential, with a static compression during the mode II cycle.

Such loading paths were experimentally reproduced using transversally precracked thin tubes of $R260$ rail steel loaded in tension-compression and torsion. The microstructure and elastic-plastic constitutive equation of this material are detailed in [23]. The yield stress is 480 MPa. The samples contain a small circular hole at mid height used as a crack starter during mode I precracking, and are covered with a speckle painting. Stereo digital image correlation is performed with the VIC3D software. The pixel size is 7 μm, with a subset size of approximatively 150 μm. The results of those experiments in terms of crack paths and kinetics will not be discussed in this paper.

The goal of the present study is rather to find the most suitable displacement field post-treatment method to accurately measure the crack length and effective SIFs during those experiments. This method has to account for non linearities: the effects of friction and contact between the crack faces as well as crack-tip plasticity.

2 Methodology

Several approaches were tested to evaluate the influence of non linearities on crack tip localization and estimation of the effective SIFs. For that purpose, displacement fields issued from finite element computations with contact/friction and/or elastic-plastic behavior, for which the exact crack-tip location and the effective SIFs are known were used. Those SIFs were computed using the relative crack face displacement jump, which allows a correct evaluation of the SIFs in the presence of contact and friction between the crack faces, contrary to classical J-integral methods. In the following, those effective SIFs will be referred to as ΔK^{FEM}. If plasticity is modeled in the computation, the SIFs are evaluated on a similar computation (loading & compression/friction), but with an elastic behavior.

The mesh and boundary conditions are represented on figure 1. The crack length is $2a = 4$ mm, and plane stress is assumed. The FEM-obtained displacement fields are projected on a square grid with a 20 μm pitch, similar to the grid used for DIC.

For mode I, the load ratio R_I was either zero or negative, depending on the computations, but the displacement fields were always extracted at maximum and minimum loads, and their difference was used to compute ΔK_I^{FEM}.

Fully reversed mode II was simulated with or without a superimposed static normal compression. Again, the displacement fields were extracted at maximum and minimum shear loads and their difference was used to compute ΔK_{II}^{FEM}.

Using Von Mises criterion and Irwin's approach for perfectly plastic materials, the extensions of the cyclic plastic zone ahead of the crack tip in plane stress for mode I and mode II are approximately:

$$r_{p,I} = \frac{1}{2\pi}\left(\frac{\Delta K_I}{2\sigma_Y}\right)^2 \tag{1}$$

$$r_{p,II} = \frac{3}{2\pi}\left(\frac{\Delta K_{II}}{2\sigma_Y}\right)^2 \tag{2}$$

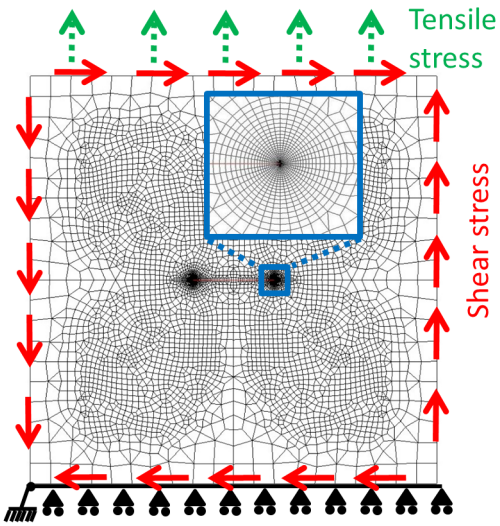

Figure 1: FEM mesh and boundary conditions. Plate size: $10 * 10$ mm^2, crack length: $2a = 4$ mm. Element size at the tip: 25 μm.

In order to allow a transposition of the results to other materials, the approximate size of the cyclic crack tip plastic zone, according to equations 1 and 2 will be specified for each mode I or mode II case analysed. But note that when real experimental mixed-mode displacement fields are analysed, due to friction stresses that reduce ΔK_{II}^{eff}, the effective size of the mode II plastic zone is not known a priori, and is often actually significantly smaller than predicted, inserting the nominal K_{II} in eq. 2 [28].

Elastic frictionless computations were performed under mode I or mode II loading. Various elastic-plastic computations were performed using constitutive equations for $R260$ rail steel [23], to study the influence of crack-tip plasticity. In that case, two cycles were simulated, which was enough to get a stabilized cycle since the hardening is mostly kinematic. Elastic computations were performed under mode I or mode II with compression and friction ($\mu = 0.5$) in order to study the influence of contact stresses.

Other cases, combining both non linearities or both modes were investigated. For sequential and 90° out-of-phase mixed-mode loading (both with $R_I = 0$ and $R_{II} = -1$), the displacement fields extracted at maximum and minimum tensile load and shear load were used to determine ΔK_I^{FEM} and ΔK_{II}^{FEM}, respectively.

3 Compared approaches

Three approaches were evaluated: the first one is based on a projection of the displacement field over William's expansion, which is the most commonly used approach, the second one is based on a fit of the relative displacement between two rows of virtual extensometers, above and below the crack, and the third one is based on a coupling between FEM computations and DIC.

3.1 William's expansion

This approach is based on the search for the crack tip position minimizing the error between the DIC field and its projection over William's expansion, which is the most common method. The algorithm used to locate the crack-tip is a pattern search algorithm [9], with an initial guess chosen after testing all the positions on a coarse grid. This approach gives both the crack tip position, and an estimation of the effective SIFs.

The algorithm and its parameters are described in Appendix A. The results for various loading cases are given in tables 2 & 3.

Table 2: Results obtained using William's expansion with PS algorithm in mode I. e stands for elastic behavior and $e-p$ for elastic-plastic behavior. Cyclic plastic zone r_p computed using eq. 1.

Material behavior	ΔK_I^{FEM} $(MPa\sqrt{m})$	r_p (μm)	Compressive stress	Error on crack tip location (μm)	estimated ΔK_I $(MPa\sqrt{m})$
e	10	/	0	0	10.1
e-p	10	17	0	7	10.1
e-p	20	69	0	33	20.3
e-p	30	155	0	74	31.1
e-p	30 + small unloading	155	0	-7	/
e	10	/	-50	-41	11.7
e	10	/	-100	-74	13.2
e	10	/	-150	-96	14.7
e	10	/	-150	Pre-determined tip	13.8

Table 3: Results obtained using William's expansion with PS algorithm in mode II. e stands for elastic behavior, $e-p$ for elastic-plastic behavior and $e-f$ for elastic with friction. Cyclic plastic zone r_p computed using eq. 2.

Material behavior	ΔK_{II}^{FEM}	r_p (μm)	Compressive stress	Error on crack tip location (μm)	estimated ΔK_{II} $(MPa\sqrt{m})$
e	10	/	0	-4	10.0
e-p	10	52	0	48	10.2
e-p	20	207	0	215	21.4
e-p	30	466	0	541	38.3
e-p	30	466	0	Pre-determined tip	48.0
e+f	6	/	-50	-78	7.8
e+f	1.9	/	-100	-278	5.3
e+f	2	/	-100	Pre-determined tip	5.0

In the elastic frictionless cases (LEFM hypothesis), the crack tip position and SIFs are predicted accurately for both modes.

In mode I, when crack-tip plasticity is present, the crack length is slightly overestimated and ΔK_I^{eff} as well, but the error, which rises with the applied loading range remains small: 3.6% for $\Delta K_I^{FEM} = 30$ $MPa\sqrt{m}$ ($K_I^{FEM}/\sigma_Y = 0.063\ \sqrt{m}$). Adding a compression phase leads to an underestimation of the crack length, and an overestimation of ΔK_I^{eff}, because the displacement field for a closed crack under compression is not described by William's expansion.

Another solution could be to capture several images during one cycle and correlate them with the image at maximum force, allowing to plot ΔK_I measured with William's expansion versus the applied load, as in [6], and then seek for the change of slope (as in the force-displacement method). But this last

method requires the capture of a lot of images and the post-treatment will be longer.

For mode II, adding crack-tip plasticity leads to an overestimation of the crack length by up to 0.5 mm as well as an overestimation of ΔK_{II}^{eff} up to 28 %, due to the elongated shape of the mode II plastic zone ahead of the tip. In mode II, the cyclic plastic zone is three times longer than in mode I for the same value of ΔK (see eq. 1 & 2), which explains the stronger effect of mode II crack tip plasticity on the crack tip localization and SIFs evaluation. Adding compression and friction leads to an underestimation of the crack length, and an overestimation of ΔK_{II}^{eff}, like for mode I.

From this first analysis, it appears that such an approach cannot be used to simultaneously locate the crack tip and determine the effective SIFs in the cases of high mode II loadings and high compression or friction between the crack faces. It can however be used to locate the crack tip in mode I if applied between two well chosen images: at maximum load, and after a small (elastic) unloading, as suggested by Decreuse et al. [21]. By doing so, the effects of crack-tip plasticity and contact forces between the crack faces (since the crack is always opened) can be avoided, as shown in table 2.

The same approach but with a fixed crack tip (which can be determined using the aforementioned technique) was evaluated, but the same problems persisted: overestimation of ΔK_{I}^{eff} in the presence of compression, and overestimation of ΔK_{II}^{eff} in the presence of high friction or high ΔK_{II}^{eff}.

An attempt was made to change the size of the area close to the crack tip which is excluded from the analysis (see Appendix A) in order to avoid the plastic zone. This was done by changing the inner radius R_{int} and outer radius R_{ext} of the considered area (Appendix A, figure 11). The results are given in table 4 for an elastic-plastic frictionless mode II computation with $\Delta K_{II}^{FEM} = 20\ MPa\sqrt{m}$. Increasing the inner or outer radius does no prevent an overestimation of the crack length nor an overestimation of the effective SIFs.

Table 4: Influence of the size of the excluded area (of radius R_{int}) around the crack tip for $\Delta K_{II}^{FEM} = 20\ MPa\sqrt{m}$ with elastic-plastic behavior. $r_p = 0.25\ mm$ computed using eq. 2

Rint (mm)	Rext location (μm)	Error on crack tip ΔK_{II} ($MPa\sqrt{m}$)	estimated
0.2	0.6	204	21.65
0.2	1.2	215	21.44
0.2	2	215	21.42
0.8	1.8	219	21.38

3.2 Relative displacement jump

The second approach supposes that the crack tip position is known (for example thanks to the aforementioned elastic unloading approach). Here, only the amplitude of the relative displacement jump profile between two rows of virtual extensometers located above and below the crack (see figure 2) is used. The distance between the crack face and the extensometers lines is chosen as $\delta = 0.2\ mm$ (slightly larger than a DIC subset which is 0.15 mm) in order to avoid DIC subsets overlapping with the crack, which makes the correlation wrong.

The opening or sliding displacement jump profile behind the crack tip can fitted with:

$$[[U_i]] = a_i\sqrt{r} + b_i \ , \ i = x, y \tag{3}$$

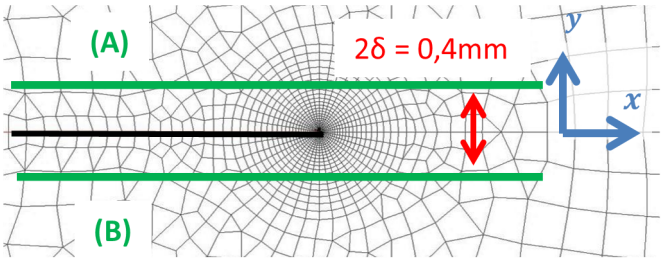

Figure 2: Lines above and below the crack between which the displacement jump is measured.

Where the offset b_i accounts for the fact that the displacements are not measured exactly along the crack faces, but at a distance δ. The effective SIFs can be deduced as:

$$\Delta K_I = a_y \frac{E\sqrt{2\pi}}{8} \ , \ \Delta K_{II} = a_x \frac{E\sqrt{2\pi}}{8} \tag{4}$$

In order to capture the influence of crack tip plasticity, it is possible to use a displacement jump profile obtained by elastic-plastic frictionless FEM computations and to apply an inverse method, as done in [2, 22, 23]. Such computations are run at various loading ranges (each one corresponding to a certain ΔK), and by finding the loading range for which the computed displacement profile fits best the measured one, one can estimate $\Delta K^{effective}$:

$$[[U_y]] = [[U_y^{Plastic}]](\Delta K_I) \tag{5}$$

$$[[U_x]] = [[U_x^{Plastic}]](\Delta K_{II}) \tag{6}$$

This method however supposes that friction does not change the shape of the displacement jump profile, but only reduces its intensity, which may not be correct. The previous displacement jump can be improved by a constant term, which will account for the friction effects. If the crack is locked, the cracked plate will behave as a crack-free plate, and the displacement jump between the two lines will be constant:

$$[[U_y]] = [[U_y^{Plastic}]](\Delta K_I) + B_I \tag{7}$$

$$[[U_x]] = [[U_x^{Plastic}]](\Delta K_{II}) + B_{II} \tag{8}$$

By finding the combination of $[[U^{Plastic}]]$ and B which gives the best fit, one is able to estimate $\Delta K^{effective}$ in the same way as before.

The results of those three approaches are given in tables 5 & 6 .

When using eq. 3, the effective SIFs are alway underestimated, which is due to the fact that the lines between which the relative displacement is measured are too far away from the crack to use such form, as explained below. The inverse method taking into account crack tip plasticity (eq. 5-6) gives good estimations in the elastic plastic cases, but overestimates the SIFs when contact stresses are added. Eq. 7-8 taking into account both crack tip plasticity and contact stresses give good estimations in every cases.

The fact that the offset in eq. 7-8 improves the results in cases with friction/contact is due to the displacement induced by the stresses transmitted through the crack faces. The higher the distance between the two rows of extensometers (2δ), the higher these displacements, and the more necessary this offset is, as illustrated by table 7. Note that this offset also depends on the level of compression (or friction).

Those approaches using the relative crack face displacement suppose that the crack tip position is known. For a 0.1 mm error on the crack tip position (either vertical or horizontal), the error on the

Table 5: Results obtained using the displacement jump approaches in mode I. e stands for elastic behavior and $e-p$ for elastic-plastic behavior.

Material behavior	ΔK^{FEM} $(MPa\sqrt{m})$	Compressive stress	Estimated ΔK_I $(MPa\sqrt{m})$		
			Analytical displacement jump	Elastic plastic	Elastic plastic + offset
e	10.0	0	7.5	/	/
e-p	30.0	0	20.9	30.0	30.0
e	10.0	-150	7.5	/	/
e-p	10.0	-100	7.2	10.8	10.2

Table 6: Results obtained using the displacement jump approaches in mode II. e stands for elastic behavior, $e-p$ for elastic-plastic behavior, $e-f$ for elastic with friction and $e-p+f$ for elastic-plastic with friction.

Material behavior	ΔK^{FEM} $(MPa\sqrt{m})$	Compressive stress	Estimated ΔK_{II} $(MPa\sqrt{m})$		
			Analytical displacement jump	Elastic plastic	Elastic plastic + offset
e	10.0	0	6.3	/	/
e-p	30.0	0	15.1	30.0	30.0
e+f	6.0	-50	3.8	/	/
e-p+f	1.9	-100	1.2	3.5	1.9

Table 7: Influence of the distance δ on the estimated SIF in mode I with 100 MPa compression and elastic-plastic behavior using no offset (eq. 5-6).

δ (mm)	0	0.05	0.1	0.2	0.5
estimated ΔK_I $(MPa\sqrt{m})$	10	10.4	10.6	10.8	11.7

estimated SIFs stays below 5%.

The approach giving the best results in pure mode I and mode II cases (eq. 7-8) was applied to non-proportional loading cases. In the case of a sequential loading path (table 8), the SIFs are evaluated accurately for $\Delta K_{I\&II} = 20\ MPa\sqrt{m}$, and are still acceptable at $\Delta K_{I\&II} = 30\ MPa\sqrt{m}$ (less than 10% error), even though the FEM-computed displacement jump profiles were obtained for pure mode I and pure mode II.

In the case of a 90° out-of-phase loading path with $R_I = 0$ and $R_{II} = -1$ (table 9), the results are acceptable at $\Delta K_{I\&II} = 20\sqrt{m}$ (less than 10% error), but not at $\Delta K_{I\&II} = 30\ MPa\sqrt{m}$. In this case, the values of $\Delta K_{I\&II}$ are overestimated, and a high $\Delta K_{II} = 15.6\ MPa\sqrt{m}$ is measured (instead of $\Delta K_{II} = 0$) by correlation of the images taken at maximum/minimum tensile stress. This is due to the fact that the FEM-computed displacement jump are obtained for pure mode I or pure mode II, instead of the real loading path, for which the couplings between tensile and shear plastic flows at the crack tip are not negligible at 0.2 mm from the crack tip for high loadings.

Table 8: Results with eq. 7-8 for sequential loadings with $R_I = 0$ and $R_{II} = -1$.

$\Delta K_{I\&II}^{FEM}$ $(MPa\sqrt{m})$	part of the cycle	Estimated ΔK_I $(MPa\sqrt{m})$	Estimated ΔK_{II} $(MPa\sqrt{m})$
20	mode I	20	0.5
	mode II	0.1	20.3
30	mode I	33	1.5
	mode II	1.2	30.4

Table 9: Results with eq. 7-8 for 90° out-of-phase loadings with $R_I = 0$ and $R_{II} = -1$.

$\Delta K_{I\&II}^{FEM}$ $(MPa\sqrt{m})$	correlated images	Estimated ΔK_I $MPa\sqrt{m}$	Estimated ΔK_{II} $MPa\sqrt{m}$
20	tensile min/max	20	2.2
	shear min/max	0.4	20.1
30	tensile min/max	32.7	15.6
	shear min/max	6.1	30.1

3.3 DIC-FEM coupling

The previous approach provides an estimate of the effective SIFs, but no information on the friction and contact forces along the crack faces.

An approach, coupling FEM computations and DIC is proposed in order to estimate both the effective SIFs and the distribution of the contact and friction stresses along the crack faces. The crack tip and path have to be determined beforehand using another approach.

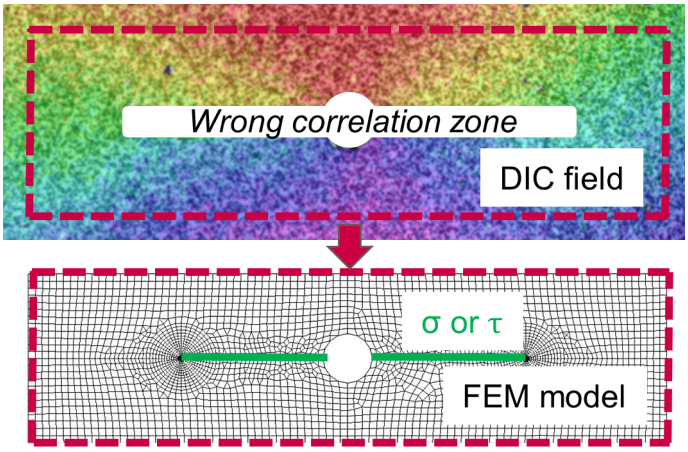

Figure 3: Principle of the DIC-FEM coupling.

The displacement is extracted on a closed contour (containing the crack) on the DIC field, as shown in figure 3, and linearly interpolated (without any noise filtering) and imposed on the nodes along the

contour of the FEM model, similarly to what is done in [29] or [30] (no interpolation in the later). The displacement field obtained by solving the FEM problem is then compared with the DIC field. If contact stresses are present between the crack faces in the experiment, and if the FEM model does not consider the possibility of friction and contact between the crack faces, those two displacement will be equal close to the contour (where the displacement is imposed), but will be different close to the crack, as shown by figure 4 a.

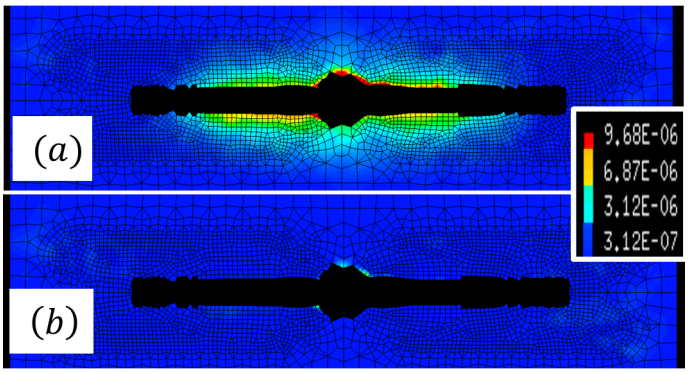

Figure 4: Quadratic error on total displacement with (a) and without (b) friction model with elastic modeling. DIC displacement field obtained experimentally for mode II loading with compression.

Contact and friction stresses along the crack faces are added in the FEM model, and their values are optimized in order to reduce the error between the DIC field and the FEM computed field, giving the results shown on figure 4 b. This idea is quite similar to the approach that Réthoré et al. [31] [32] used in order to obtain several material parameters by performing a single tensile test with DIC on a plate with a hole, or to the approach used by Blaysat et al. [33] to identify the cohesive traction profile for interface debonding.

Those contact/friction forces are modeled as piecewise affine. The values on each regularly-spaced points (spacing of 1 mm) are optimized in order to minimize the quadratic error between the DIC field and the FEM field on an area excluding points that are too close to the crack faces (where the DIC field is wrong), as in figure 3. The problem can be written as:

$$\{\sigma_l\} = ArgMin\left(\sqrt{\int\int(\underline{U}_{DIC} - \underline{U}_{FEM}(\sigma_l))^2}\right) \tag{9}$$

Where σ_l is the contact and friction stresses profile along the crack faces. The material behavior can be elastic, or elastic plastic. In the elastic case, the principle of superposition can be used, and the FEM field can be written as:

$$\underline{U}_{FEM}(\sigma_l, BC_{DIC}) = \underline{U}_{FEM}(\sigma_l = 0, BC_{DIC}) + \sum_i \sigma_{l,i} * \underline{U}_{FEM}(\sigma_{l,i} = 1, \sigma_{l,j\neq i} = 0, BC_{DIC} = 0) \tag{10}$$

Where $\sigma_{l,i}$ is the contact/friction stress at point i of the piecewise affine contact stresses profile, and BC_{DIC} denote the DIC-obtained Dirichlet boundary conditions. The solution of eq. 9 is then:

$$\{\sigma_l\} = [[B]^T[B]]^{-1}[B]^T\left(\underline{U}_{DIC} - \underline{U}_{FEM}(\sigma_l = 0, BC_{DIC})\right) \tag{11}$$

With:

$$[B] = [\underline{U}_{FEM}(\sigma_{l,i} = 1, \sigma_{l,j\neq i} = 0, BC_{DIC} = 0)] \tag{12}$$

This method has been applied on displacements fields obtained from elastic-plastic computations, and the results are given in tables 10 & 11 column 'Elastic'. In mode I, this method gives an acceptable estimation of $\Delta K_I^{effective}$ for every loading. In mode II, $\Delta K_{II}^{effective}$ is estimated accurately below 10

$MPa\sqrt{m}$ and overestimated above this amplitude.A few computed contact/friction stresses profiles are plotted on figure 5. These profiles are well estimated in mode I & mode II below 10 $MPa\sqrt{m}$, but not above, due to the fact that the algorithm tries to compensate the influence of crack tip plasticity by changing the contact stress profile.

Table 10: Results obtained using the DIC-FEM approaches in mode I. All displacement fields are obtained from elastic plastic computations.

ΔK_I^{FEM} $(MPa\sqrt{m})$	Compressive stress (MPa)	Estimated ΔK_I $(MPa\sqrt{m})$		
		Elastic	Plastic Dirichlet	Plastic Neumann
10	0	10.1	9.9	9.8
10	100	10.5	10.3	10.3
30	0	33.2	31.4	26.6

Table 11: Results obtained using DIC-FEM approaches in mode II. All displacement fields are obtained from elastic plastic computations.

ΔK_{II}^{FEM} $(MPa\sqrt{m})$	Compressive stress (MPa)	Estimated ΔK_{II} $(MPa\sqrt{m})$		
		Elastic	Plastic Dirichlet	Plastic Neumann
10	0	10.8	10.2	9.8
20	0	27.1	21.9	17.7
30	0	61.6	39.3	23.2
1.9	100	1.9	1.8	1.8

In order to avoid this artefact, the same problem (eq 9) is iteratively solved with an elastic-plastic behaviour. Since the superposition principle cannot be used any more, the problem is solved using a Levenberg Marquardt's algorithm. The damping parameter is increased by a factor 5 / decreased by a factor 2 if the current step gives a lower / higher residual than the previous.

Once the contact/friction stresses along the crack faces σ_l are known, the effective SIFs can be estimated with an elastic computation, using the relative opening and sliding displacement profiles (SIF procedure in CAST3M FE code). In this elastic computation, the boundary conditions on the outside contour can be either Dirichlet (extracted from DIC) or Neumann (stresses extracted from the elastic-plastic computations). Results are given in tables 10 & 11, columns 'Plastic Dirichlet' and 'Plastic Neumann'.

In mode I, $\Delta K_I^{effective}$ is estimated accurately. In mode II, $\Delta K_{II}^{effective}$ is estimated accurately below 20 $MPa\sqrt{m}$. Above this amplitude, it is overestimated when Dirichlet BC are used for the SIFs computation, while it is underestimated when Neumann's BC are used. This error is due to the fact that the crack-tip plastic zone is so elongated ahead of the crack tip that it extend beyond the model's contour.

Taking into account the elastic-plastic behaviour improves the contact/friction stress profile estimation compared to the elastic resolution, as seen on figure 5. Even for $\Delta K_{II}^{effective} = 20\ MPa\sqrt{m}$, the error on the estimated frictional stress is below 7 MPa.

This contact/friction stress profile is quite sensitive to noise. Adding a white Gaussian noise with a Signal to Noise Ratio of 100 ($SNR = \Sigma U_{signal}^2 / \Sigma U_{noise}^2$) leads to a standard deviation of 16.8 MPa, with a maximum error of 37 MPa, as shown in table 12 for a discretization of contact stresses σ_l every

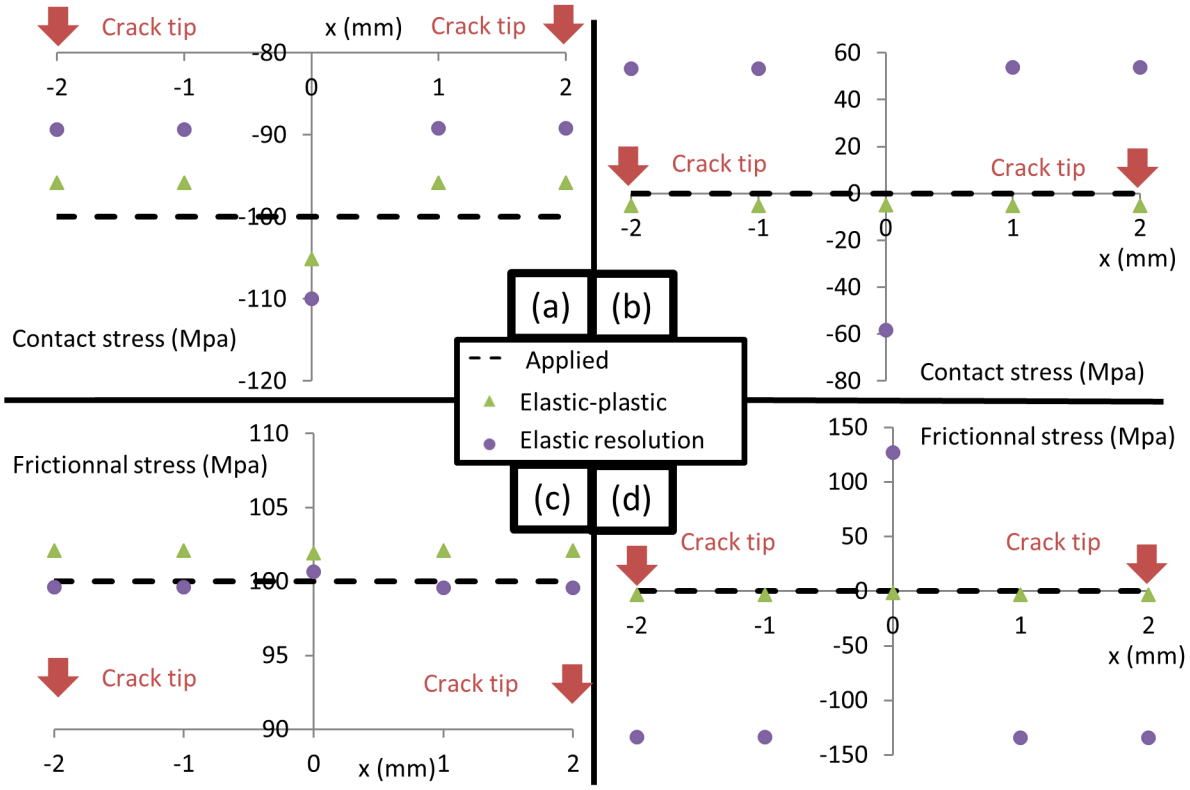

Figure 5: Estimated profile of the contact/friction stresses along the crack faces, for the hole-free model shown on figure 1. (a): Mode I $\Delta K_I^{FEM} = 10\ MPa\sqrt{m}$, 100 MPa compression. (b) Mode I, $\Delta K_I^{FEM} = 30\ MPa\sqrt{m}$, no compression. (c): Mode II $\Delta K_{II}^{FEM} = 1.9\ MPa\sqrt{m}$, 100 MPa friction. (d): Mode II $\Delta K_{II}^{FEM} = 20\ MPa\sqrt{m}$, no friction.

1 mm. A window average, similar to that induced by DIC (150 μm subset size) has no effects on the computed stress profile (less than 1 MPa difference with raw FEM field). This limited effect might be due to the large exclusion area (200 μm), outside of which the displacement gradient and thus the effect of the window average is lower. A finer discretization of contact stresses (every 0.5 mm, and thus an increase of the number of variables) increased the errors on the computed stresses. A compromise has thus to be found between resolution and noise sensitivity.

~~However, all those parameters (noise, window average and discretization pitch) have little influence on the estimated ΔK^{eff}, as the contact/friction stress profile is, in average, close to the expected profile. Most of the errors on the SIFs reported in table 12 are due to a plastic zone extending beyond the model's contour for the computation at $\Delta K_{II} = 20\ MPa\sqrt{m}$.~~

In the case of sequential and 90° out-of-phase loadings, the same type of problem as with the previous approach occurs: when the couplings between shear and tensile plastic flows at the crack tip becomes non negligible, some mode I is measured between images where only mode II should be present (and vice versa).

4 Application on experimental displacement fields

The previous approaches were applied on experimental data in order to estimate their robustness. A transversally precracked R260 rail steel tube was submitted to mode I cycles with a fixed maximum load of 10 kN (133 MPa) and various minimum loads, ranging from -5 kN to 8 kN. Images were captured

Table 12: Influence of noise (SNR = signal to noise ratio), window average of 150 μm (WA) and discretization of the piecewise affine function σ_l on the results of the 4 computations proposed in figure 5.

Noise / Window average	Discretization of σ_l (mm)	Max error on σ_l (MPa)	Standard deviation on σ_l (MPa)	Max error on ΔK^{eff} $(MPa\sqrt{m})$	Standard deviation on ΔK^{eff} $(MPa\sqrt{m})$
None	1	6.7	4.3	1.9	1.2
SNR 100	1	36.8	16.8	3.1	1.6
WA	1	7.3	4.5	1.9	1.2
None	0.5	14.9	5.9	2.0	1.2
SNR 100	0.5	54.9	22.7	3.6	1.9
WA	0.5	14.7	6.0	2.0	1.2

periodically during those cycles.

Fully reversed mode II cycles with various amplitudes and various superimposed static tensile or compressive axial load were also run, with periodic image capture. Between two consecutive shear load amplitudes, the crack was opened by applying a 10 kN tensile load in order to eliminate any residual friction/asperities interlocking.

The crack tip was located using the projective approach with William's expansion between the images at 0 and 10 kN. The effective SIFs were then estimated using a fixed crack tip with a projection over William's expansion, the fit of the displacement jump profile with eq 7-8 and the DIC-FEM approach with elastic-plastic behavior and SIFs computed using Dirichlet boundary conditions.

$\Delta K_I^{effective}$ was estimated using those three approaches on DIC fields obtained between an image at maximum tensile force (10 kN) and images at lower forces. The results are given on figure 6. When the minimum tensile stress is larger than 27 MPa ($R > 0.2$), the three approaches gives the same results. Under this value, the crack closes and both the DIC-FEM and Displacement jump profile approaches gives the same $\Delta K_I^{effective}$, which remains constant as the crack goes into compression. As predicted from the tests on FEM computed fields, the $\Delta K_I^{effective}$ estimated using the projection over William's expansion increases when the crack is closed and under compression, and is thus overestimated. The same type of phenomena can be seen in figure 6.d. of [11] on a projective approach and a COD approach.

$\Delta K_{II}^{effective}$ was estimated using those three approaches on DIC fields obtained between images captured at maximum/minimum shear loads, for various loading ranges with a 66 MPa static compression.The results are given in figure 7. The DIC-FEM and displacement jump profile approaches give the same $\Delta K_{II}^{effective}$, while the projection over William's expansion gives a higher estimation of $\Delta K_{II}^{effective}$: as expected from the tests on FEM computed fields, this approach overestimates $\Delta K_{II}^{effective}$ in the presence of high friction between the crack faces. $\Delta K_{II}^{effective}$ was below 15 $MPa\sqrt{m}$ and the influence of crack tip plasticity on this last approach was thus negligible.

$\Delta K_{II}^{effective}$ was estimated using those three approaches on DIC fields obtained between images captured at maximum/minimum shear loads, at various crack lengths with a 53 MPa static tension so that the crack was opened and frictionless. The results are given in figure 8. When the crack is short, the three approaches give the same $\Delta K_{II}^{effective}$ ($\approx$ 15 $MPa\sqrt{m}$). As the crack propagates, the SIFs increases and the projection over William's expansion gives a higher $\Delta K_{II}^{effective}$ than the other two approaches (which takes into account crack-tip plasticity), as predicted from the tests on FEM computed fields.

The DIC-FEM coupling method with elastic-plastic computations was used to obtain the friction and contact stresses profiles along the crack faces (see figures 9 a&b). As expected, for mode II loading (figure

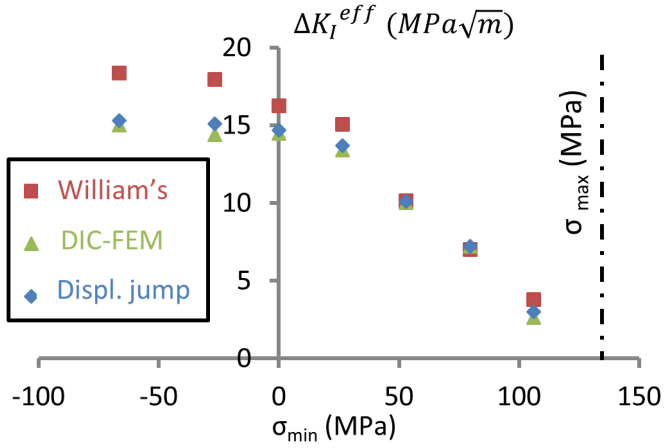

Figure 6: Estimated ΔK_I in pure mode I, at fixed σ_{max} (133 MPa) for various σ_{min}.

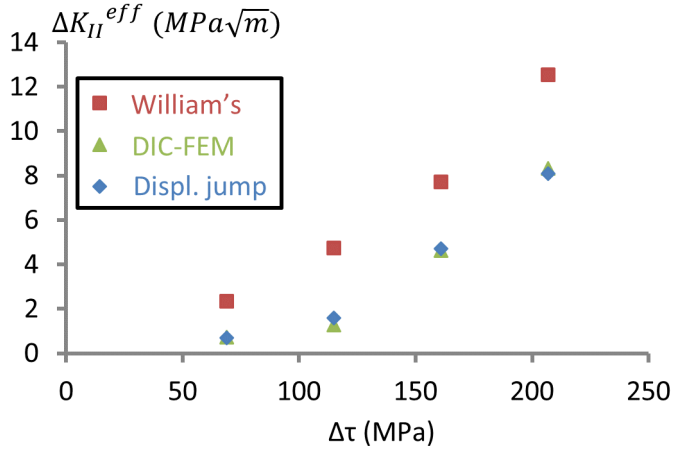

Figure 7: Estimated ΔK_{II} for various shear stress ranges and -5 kN (-66 MPa) static compression.

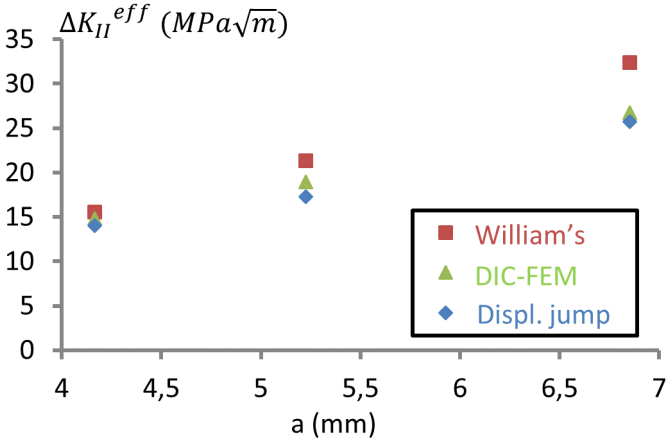

Figure 8: Estimated ΔK_{II} for various crack length at fixed $\Delta\tau = 115$ MPa with a 4 kN (53 MPa) static tension.

9.a), a static compression enhances crack face friction, which rises with the distance to the crack tip. The stress concentration due to the central hole does not seem to explain this tendency, because it drops much faster than the computed friction stress. Note that friction is still present without any far-field compression, and even when a slight opening stress is present ($K_I = 3.3\ MPa\sqrt{m}$), which is either due to crack face roughness or an artifact due to noise.

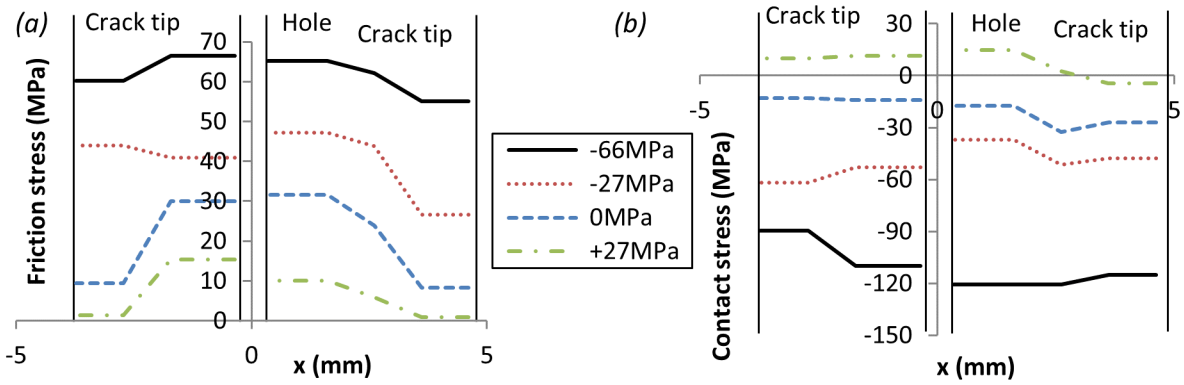

Figure 9: Estimated friction stress profile at fixed $\Delta\tau = 115\ MPa$ with various static tensile or compressive loads (a). Estimated contact stress profile in mode I at fixed σ_{max} (133 MPa) for various σ_{min} (b)

For mode I loading at negative R ratio (figure 9.b), the computed contact stresses are higher than the minimal far-field stress, and even for $R = 0$, contact stresses are still present, which is either due to closure effects or an artifact due to noise. The second interpretation seems more plausible, since slightly positive "contact stresses", which have no physical meaning, are obtained for a 27 MPa minimal tensile load ($R = 0.2$).

5 Conclusions

The widely used method of projecting the DIC field over William's expansion, coupled with a grid search and a Pattern Search algorithm allows an accurate estimation of the crack tip position and effective SIFs when crack tip plasticity is limited and when no contact stresses are present along the crack faces. For high loading ranges, especially in mode II, the crack length is overestimated due to the elongated plastic zone ahead of the crack tip, while high contact stresses between the crack faces lead to an underestimation of the crack length. Both effects leads to an overestimation of the effective SIFs, even if the datapoints located in the plastic zone are excluded. This method can nonetheless still be used to locate the crack tip in mode I by applying it to images captured at maximum load and after a small elastic unloading.

An inverse analysis of the measured relative displacement jump profile compared to the profile obtained from an elastic-plastic computation plus an offset gives a better estimation of the effective SIFs when non linearities are present. It captures the effect of crack-tip plasticity as well as the effect of contact stresses between the crack faces for pure mode I, pure mode II and sequential loadings, which William's expansion cannot do. For 90° out-of-phase mixed-mode loading, it can be used until the coupling between shear and tensile plastic flows at the crack tip becomes non negligible.

An approach coupling DIC and FEM computations is proposed to evaluate the effective SIFs and the contact stresses along the crack faces. Although giving accurate results in terms of effective SIFs on FE-generated displacement fields, and providing estimates of the profile of contact and friction stresses along the crack faces, this method is much more sensitive to noise and time consuming ($\approx 5\ hours$) than the aforementioned inverse approach (a few seconds).

Overall, the second approach provides the best compromise between accuracy and efficiency, at least until the FEM-DIC method has been improved to reduce its noise sensitivity.

Acknowledgements

The authors would like to acknowledge SNCF for its financial support.

Appendices

A PS algorithm with William's expansion

The algorithm used to determine the crack tip and effective SIFs using a projection (which is equivalent to a minimization in terms of least square error) over William's expansion is described in figure 10. At each possible crack tip location, only a part of the DIC field is used, as shown on figure 11. *Rint* is chosen sufficiently large to avoid DIC elements which are overlapping the crack and for which the correlation is wrong. The algorithm is a mix between the grid search of [10] and the PS algorithm of [9], where the minimization function is the Euclidean distance:

$$\|\underline{U}_{William's} - \underline{U}_{DIC}\|_2 = \sqrt{\sum_{n=0}^{N} (U_{William's,\,n} - U_{DIC,\,n})^2} \tag{13}$$

With N the number of points in the considered area.

In this study, the crack orientation is supposed to be known, although it is possible to modify the PS algorithm to add a search over the crack angle (and not only over the crack tip position), which is out of the scope of this study.

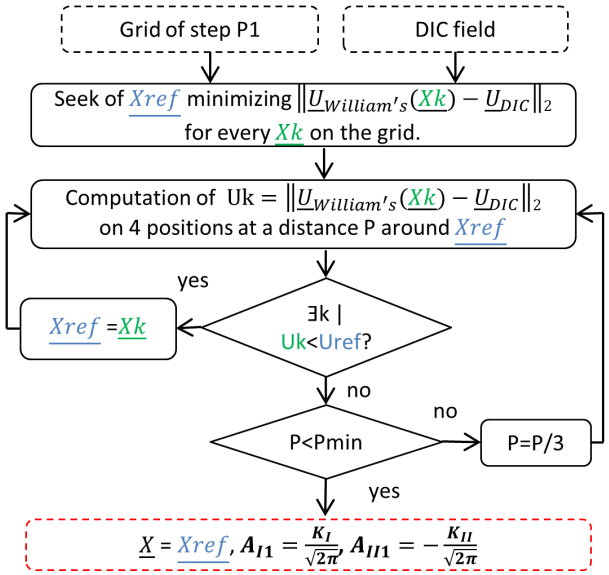

Figure 10: PS algorithm with William's expansion. $\underline{Xref}$ represents the current supposed crack tip and $\underline{Xk}$ the tested crack tip positions.

Noting the horizontal and vertical displacements u_x and u_y respectively, with G the shear modulus and $k = (3-\nu)/(1+\nu)$ (plane stress hypothesis), William's expansion writes:

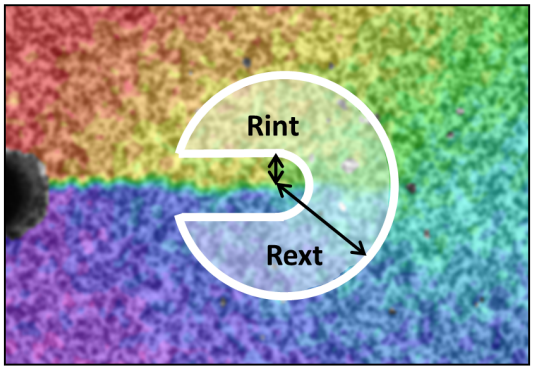

Figure 11: Example of measured opening displacement field and Shape of the zone used in the PS algorithm. $Rext = 1.2\ mm$ and $Rint = 0.2\ mm$.

$$
\begin{aligned}
u_x = &\sum_{n=0}^{N} \frac{A_I^n}{2G} r^{\frac{n}{2}} \left((\kappa + \frac{n}{2} + (-1)^n) cos(\frac{n}{2}\theta) - \frac{n}{2} cos((\frac{n}{2} - 2)\theta) \right) \\
&+ \sum_{n=0}^{N} \frac{A_{II}^n}{2G} r^{\frac{n}{2}} \left((-\kappa - \frac{n}{2} + (-1)^n) sin(\frac{n}{2}\theta) + \frac{n}{2} sin((\frac{n}{2} - 2)\theta) \right)
\end{aligned} \tag{14}
$$

$$
\begin{aligned}
u_y = &\sum_{n=0}^{N} \frac{A_I^n}{2G} r^{\frac{n}{2}} \left((\kappa - \frac{n}{2} - (-1)^n) sin(\frac{n}{2}\theta) + \frac{n}{2} sin((\frac{n}{2} - 2)\theta) \right) \\
&+ \sum_{n=0}^{N} \frac{A_{II}^n}{2G} r^{\frac{n}{2}} \left((\kappa - \frac{n}{2} + (-1)^n) cos(\frac{n}{2}\theta) + \frac{n}{2} cos((\frac{n}{2} - 2)\theta) \right)
\end{aligned} \tag{15}
$$

The rigid body translations t_x and t_y are contained in the order 0 terms:

$$t_x = \frac{A_I^0}{2G}(\kappa + 1) = \frac{4A_I^0}{E} \tag{16}$$

$$t_y = \frac{A_{II}^0}{2G}(\kappa + 1) = \frac{4A_{II}^0}{E} \tag{17}$$

The stress intensity factors are contained in the order 1 terms:

$$K_I = \sqrt{2\pi} A_I^1 \tag{18}$$

$$K_{II} = -\sqrt{2\pi} A_{II}^1 \tag{19}$$

The rigiby body rotation Ω and the T-stress T are contained in the order 2 terms:

$$\Omega = \frac{A_{II}^2}{2G}(\kappa + 1) = \frac{4A_{II}^2}{E} \tag{20}$$

$$T = \frac{A_I^2}{2G}(\kappa + 1)E = 4A_I^2 \tag{21}$$

The parameters used in this study are: $R_{int} = 0.2\ mm$, $R_{ext} = 1.2\ mm$, grid step $P_1 = 0.1\ mm$, PS algorithm steps from $P = 0.033\ mm$ to $P = 0.0037$, order of the William's expansion terms: from 0 to 7. Using those parameters, the time to process one DIC field is about 5 to 10 seconds. Each projection over William's expansion is extremely fast since it only needs to invert a $16 * 16$ matrix and build/multiply some $n * n$ matrix, n being the number of points in the projection zone.

References

[1] M C Smith and R A Smith. Toward an understanding of mode II fatigue crack growth. Basic Questions in Fatigue, 1:260–280, 1988.

[2] G. Bertolino and V. Doquet. Derivation of effective stress intensity factors from measured crack face displacements. Eng Fract Mech, 76:1574–1588, 2009.

[3] D. B. Barker, R. J. Sanford, and R. Chona. Determining K and related stress-field parameters from displacement fields. Experimental Mechanics, 25:399–407, 1985.

[4] Jorge Abanto-Bueno and John Lambros. Investigation of crack growth in functionally graded materials using digital image correlation. Eng Fract Mech, 69(14-16):1695–1711, 2002.

[5] J. R. Yates, M. Zanganeh, and Y. H. Tai. Quantifying crack tip displacement fields with DIC. Eng Fract Mech, 77:2063–2076, 2010.

[6] J. Tong, S. Alshammrei, T. Wigger, C. Lupton, and J. R. Yates. Full-field characterization of a fatigue crack: Crack closure revisited. FFEMS, 41:2130–2139, 2018.

[7] Stéphane Roux and François Hild. Stress intensity factor measurements from digital image correlation: Post-processing and integrated approaches. Int J Fracture, 140(1-4):141–157, 2006.

[8] S. Yoneyama, T. Ogawa, and Y. Kobayashi. Evaluating mixed-mode stress intensity factors from full-field displacement fields obtained by optical methods. Eng Fract Mech, 74:1399–1412, 2007.

[9] M. Zanganeh, P. Lopez-Crespo, Y. H. Tai, and J. R. Yates. Locating the crack tip using displacement field data: A comparative study. Strain, 49:102–115, 2013.

[10] R. Harilal, C. P. Vyasarayani, and M. Ramji. A linear least squares approach for evaluation of crack tip stress field parameters using DIC. Optics and Lasers in Engineering, 75:95–102, 2015.

[11] Michael Vormwald, Yigiter Hos, José L.F. Freire, Giancarlo L.G. Gonzáles, and Jorge G. Díaz. Crack tip displacement fields measured by digital image correlation for evaluating variable mode-mixity during fatigue crack growth. Int J Fatigue, 115:53–66, 2018.

[12] P Lopez-Crespo, A Shterenlikht, E A Patterson, J R Yates, and P J Withers. The stress intensity of mixed mode cracks determined by digital image correlation. The Journal of Strain Analysis for Engineering Design, 43:769–780, 2008.

[13] P. Lopez-Crespo, A. Shterenlikht, J. R. Yates, E. A. Patterson, and P. J. Withers. Some experimental observations on crack closure and crack-tip plasticity. FFEMS, 32:418–429, 2009.

[14] R Hamam, F. Hild, and S. Roux. Stress intensity factor gauging by digital image correlation: Application in cyclic fatigue. Strain, 43(October 2006):181–192, 2007.

[15] F Mathieu, F Hild, and S Roux. Identication of a crack propagation law by digital image correlation. Int J Fatigue, 36:146–154, 2012.

[16] J. Réthoré, A. Gravouil, F. Morestin, and A. Combescure. Estimation of mixed-mode stress intensity factors using digital image correlation and an interaction integral. Int J Fracture, 132(1):65–79, 2005.

[17] Julien Réthoré, Stéphane Roux, and François Hild. Noise-robust stress intensity factor determination from kinematic field measurements. Eng Fract Mech, 75:3763–3781, 2007.

[18] Yigiter Hos, José L F Freire, and Michael Vormwald. Measurements of strain fields around crack tips under proportional and non-proportional mixed-mode fatigue loading. Int J Fatigue, 2016.

[19] S L Wong, P E Bold, M W Brown, and R J Allen. A branch criterion for shallow angled rolling contact fatigue cracks in rails. Wear, 191:45–53, 1996.

[20] S L Wong, P E Bold, M W Brown, and R J Allen. Two measurement techniques for determining effective stress intensity factors. FFEMS, 23:659–666, 2000.

[21] P. Y. Decreuse, S. Pommier, M. Poncelet, and B. Raka. A novel approach to model mixed mode plasticity at crack tip and crack growth. Experimental validations using velocity fields from digital image correlation. Int J Fatigue, 42:271–283, 2012.

[22] V. Doquet, Q. H. Bui, G. Bertolino, E. Merhy, and L. Alves. 3D shear-mode fatigue crack growth in maraging steel and Ti-6Al-4V. Int J Fracture, 165:61–76, 2010.

[23] Thomas Bonniot, Véronique Doquet, and Si Hai Mai. Mixed mode II and III fatigue crack growth in a rail steel. Int J Fatigue, 115(October 2018):42–52, 2018.

[24] Joël Lachambre, Julien Réthoré, Arnaud Weck, and Jean Yves Buffiere. Extraction of stress intensity factors for 3D small fatigue cracks using digital volume correlation and X-ray tomography. Int J Fatigue, 71:3–10, 2015.

[25] S. Pommier, C. Prioul, and P. Bompard. Influence of a negative R ratio on the creep-fatigue behaviour of the N18 nickel base superalloy. FFEMS, 20(1):93–107, 1997.

[26] S Bogdanski, M Olzak, and J Stupnicki. Numerical modelling of a 3d rail rcf 'squat'-type crack under operating load. FFEMS, 21:923–935, 1998.

[27] S H Mai, A Gravouil, M L Nguyen-Tajan, and B Trolle. Numerical simulation of rolling contact fatigue crack growth in rails with the rail bending and the frictional contact. Eng Fract Mech, 174:196–206, 2017.

[28] T. Vojtek and M. Hrstka. How to get a correct estimate of the plastic zone size for shear-mode fatigue cracks? Theor Appl Fract Mec., 2019.

[29] J. Hosdez, M. Langlois, J-F. Witz, N. Limodin, D. Najjar, E. Charkaluk, P. Osmond, A. Forre, and F. Szmytka. Plastic zone evolution during fatigue crack growth: Digital image correlation coupled with finite elements method. Int J Solids Struct., 171:92–102, 2019.

[30] B. Lin, S. Alshammrei, and J. Tong. Characterisation of fatigue crack tip field in the presence of significant plasticity. Theor Appl Fract Mec., 103, 2019.

[31] Julien Réthoré. A fully integrated noise robust strategy for the identification of constitutive laws from digital images. Int J Numer Meth Eng, 84:631–660, 2010.

[32] Julien Réthoré, Muhibullah, Thomas Elguedj, Michel Coret, Philippe Chaudet, and Alain Combescure. Robust identification of elasto-plastic constitutive law parameters from digital images using 3D kinematics. Int J Solids Struct., 50:73–85, 2013.

[33] B. Blaysat, J.P.M. Hoefnagels, G. Lubineau, M. Alfano, and M.G.D. Geers. Interface debonding characterization by image correlation integrated with Double Cantilever Beam kinematics. Int J Solids Struct., 55:79–91, 2015.